Angewandte Chemie
Eine Zeitschrift der Gesellschaft Deutscher Chemiker

Supporting Information

69451 Weinheim, Germany

Probing Transient Conformational States of Proteins by Solid-State $R_{1\rho}$ Relaxation-Dispersion NMR Spectroscopy**

*Peixiang Ma, Jens D. Haller, Jérémy Zajakala, Pavel Macek, Astrid C. Sivertsen, Dieter Willbold, Jérôme Boisbouvier, and Paul Schanda**

anie_201311275_sm_miscellaneous_information.pdf

Supporting Information

Table of Contents

Sample preparation **2**

NMR spectroscopy, data analysis and numerical simulations **3**

Figure S1. Numerical simulations of $R_{1\rho}$ relaxation dispersion in a solid sample undergoing two-site conformational exchange and magic-angle spinning. **5**

Figure S2, Part 1. Selected time-domain data of the numerical simulations. **6**

Figure S2, Part 2. Selected time-domain data of the numerical simulations. **7**

Figure S3. Comparison of Bloch-McConnell- and MAS-simulations. **8**

Figure S4. Pulse sequence used in this study. **9**

Figure S5. Experimental RD profiles for all observed resolved correlation peaks in ubiquitin, measured at 39.5 kHz MAS frequency. **10**

Figure S6. Experimental RD profiles for all observed resolved correlation peaks in ubiquitin, measured at 20 kHz MAS frequency. **11**

Figure S7. Examples of experimental ^{15}N $R_{1\rho}$ decay curves. **12**

Figure S8. Bloch-McConnell fits of CPMG and $R_{1\rho}$-derived relaxation dispersion profiles **13**

Figure S9. Comparison of crystal structures of ubiquitin. **14**

Figure S10. Comparison of ^{15}N R_2 and $R_{1\rho}$ rates in microcrystalline ubiquitin. **15**

Table S1. Fitted exchange parameters. **16**

References **17**

Sample preparation

Ubiquitin preparation.

Uniformly $^{2}H,^{15}N$ labeled ubiquitin was expressed in E. coli BL21(DE3) cells, using D_2O-based M9 medium with 2g/L $^{2}H,^{12}C$-labeled glucose as the sole carbon source, and 1g/L $^{15}NH_4Cl$ as nitrogen source. Purification followed well-established protocols, including ion exchange and size exclusion chromatographies. For re-protonation of exchangeable sites, ubiquitin was placed in H_2O/D_2O mixtures, and the pH was raised to pH 10. Exchange was allowed to take place for 1 week, which is sufficient to exchange all amides. The H_2O/D_2O ratio was 1:1 for the sample measured at fast-MAS, and 1:4 for the sample measured at 20kHz MAS. Ubiquitin was then crystallized using 2-methylpentane-2,5-diol (MPD) as a crystallization agent, as described previously.[1]

NMR spectroscopy, data analysis and numerical simulations

All experiments were performed on a Agilent 600 MHz spectrometer equipped with a 1.6 mm MAS probe tuned to ^{1}H, ^{13}C and ^{15}N frequencies (for measurements at ~39 kHz MAS) or a 3.2 mm HXY MAS probe tuned to ^{1}H, ^{13}C and ^{15}N frequencies (for experiments at 20 kHz MAS). The MAS frequencies were stable to within 15 Hz. The pulse sequence used for all experiments is shown in Figure S4. The sample temperature was set to 300 K; this takes into account sample heating by rotation. The temperature was calibrated using the temperature-dependence of the water resonance, relative to internal DSS standard. Temperature calibration was also checked using the ^{79}Br shift in an external KBr standard,[2] and was found to match the water-based value to less than 2 degrees. The effect of the ^{15}N spin-lock field on the temperature was checked by observing the water resonance position as a function of the duration and amplitude of the ^{15}N rf field, and was found to be below 2 K in all the cases that were used in the measurements of the reported protein $R_{1\rho}$ values. The cooling temperature was adjusted accordingly.
The calibration of the ^{15}N rf field strength was done using a ^{15}N spinlock (akin to the pulse sequence in Figure S4), followed by a nutation pulse which had a 90°-shifted phase. The duration of this pulse was varied, and the zero-crossing of the signal is observed when the nutation pulse corresponds to a $\pi/2$ pulse. The spin-lock and nutation pulse amplitudes in this procedure were chosen close to the values that were finally used for the $R_{1\rho}$ experiments (in the range 5-15 kHz, several calibrations were performed). We find that this calibration is more accurate than searching the rotary-resonance condition, i.e. searching the minimum signal obtained after a spinlock that has a field strength to the MAS frequency. In addition, searching the rotary resonance condition does not allow to calibrate the field which is finally used, but only allows finding the rf field strength corresponding to the MAS frequency (i.e. the field at the n=1 rotary resonance), which in fast-MAS experiments is far from the rf fields used for the final $R_{1\rho}$ experiments.

For $R_{1\rho}$ measurements at 20 kHz MAS, eleven different spin-lock pulse durations, from 100 µs to 80 ms were used, for each of the 6 rf field strengths. The maximum indirect ^{15}N chemical shift evolution period was 17ms, and the recycle delay was 1.4s, resulting in an experimental time of 5.75 hours for one set of eleven spin-lock pulse durations.
For measurements at 39.5kHz MAS, ten different spin-lock durations were used, from 5 to 250 ms, for each of the 10 rf field strengths. One measurement series (at one rf field strength) lasted for 10.5 hours.

Standard data processing was performed with nmrPipe,[3] and involved linear prediction along the ^{15}N dimension, zero-filling and solvent-signal suppression with nmrPipe's SOL routine. All data were analyzed with nmrView (oneMoon Scientific, Inc.). Peak integrals were obtained by summation over rectangular boxes, and were then fitted with a mono-exponential (2-parameter) function, using in-house written programs in python language. Representative examples of decay curves are shown in Figure S7. Error margins on the experimental fit parameters were obtained via Monte-Carlo routines.[4] The experimental noise of the peak integrals was obtained from the

standard deviation of the spectral noise: in order to obtain error bars on integrals (summed over the integration boxes), the intensity-based noise (multiplied by 3) was multiplied by the square root of the number of points that were summed up for computing the peak integral.

On-resonance $R_{1\rho}$ relaxation rates, corresponding to R_2, were computed from $R_{1\rho}$ and R_1 as:[5]

$$R_{1\rho,\text{on-res}} = R_{1\rho,\text{measured}} / \sin^2\theta - R_1 / \tan^2\theta,$$

where θ is the angle of the effective field in the laboratory frame, i.e θ=90 degrees for an on-resonance peak.
R_1 rate constants have been published elsewhere.[6] Note that the R_1 rate constants are very small as compared to $R_{1\rho}$. Consequently, the difference between $R_{1\rho}$ and R_2 is very small.

For Bloch-McConnell fits of the data in Figure 2, the Bloch-McConnell equations for two-site exchange, as shown e.g. in reference [7] (eq. 2 there), were solved numerically. Likewise, fits of CPMG data used the numerical solution of the Bloch-McConnell equations, as done previously.[8] Error margins on the exchange parameters were obtained from 200 Monte-Carlo runs.

Numerical simulations of $R_{1\rho}$ RD profiles (as shown in Figures 1, 2b and S1 – S3) were performed using the software framework GAMMA.[9] A composite Liouville space composed of two exchanging components was used for the simulation, where the two sub-spaces corresponding to the two exchanging states are connected by exchange rate constants. Other simulation parameters followed the usual approaches for simulations in MAS ssNMR, including piecewise constant Hamiltonians[10,11] and powder averaging.[12] One-hundred powder points were used for powder averaging. The evolution of the N_x operator under spin-lock, MAS and exchange was simulated for 80 ms (for the curves shown in Figure 2b), or 200 ms (for data shown in Figure 1), and the time-domain traces were fitted to mono-exponential functions using python programs.
The ^{1}H and ^{15}N CSA tensors were assumed to be axially symmetric. The values of the anisotropies of these tensors were chosen as $\Delta\sigma = \sigma_{zz}-\sigma_{xx} = -170$ ppm for ^{15}N and $\Delta\sigma = 8$ ppm for ^{1}H. The simulations were performed for a static magnetic field strength of 14.1 T (600 MHz ^{1}H Larmor frequency), and the CSA tensor values in Hertz were obtained accordingly. The ^{1}H-^{15}N dipolar coupling was set to 20 kHz (corresponding to a bond length of 1.02Å and an order parameter of S=0.87). The ^{15}N CSA was assumed to be collinear with the NH bond. In simulations where the NH bond was assumed to be re-oriented by the exchange process (all simulations where $\theta>0°$, e.g. red curves in Figure 1), the N-H bond and the ^{15}N and ^{1}H CSAs were assumed to jump simultaneously by an angle θ.
Three-spin systems (containing an additional proton spin) were performed by keeping a remote proton at a fixed position, as shown in Figure S1.
Representative time-domain data are shown in Figure S2.

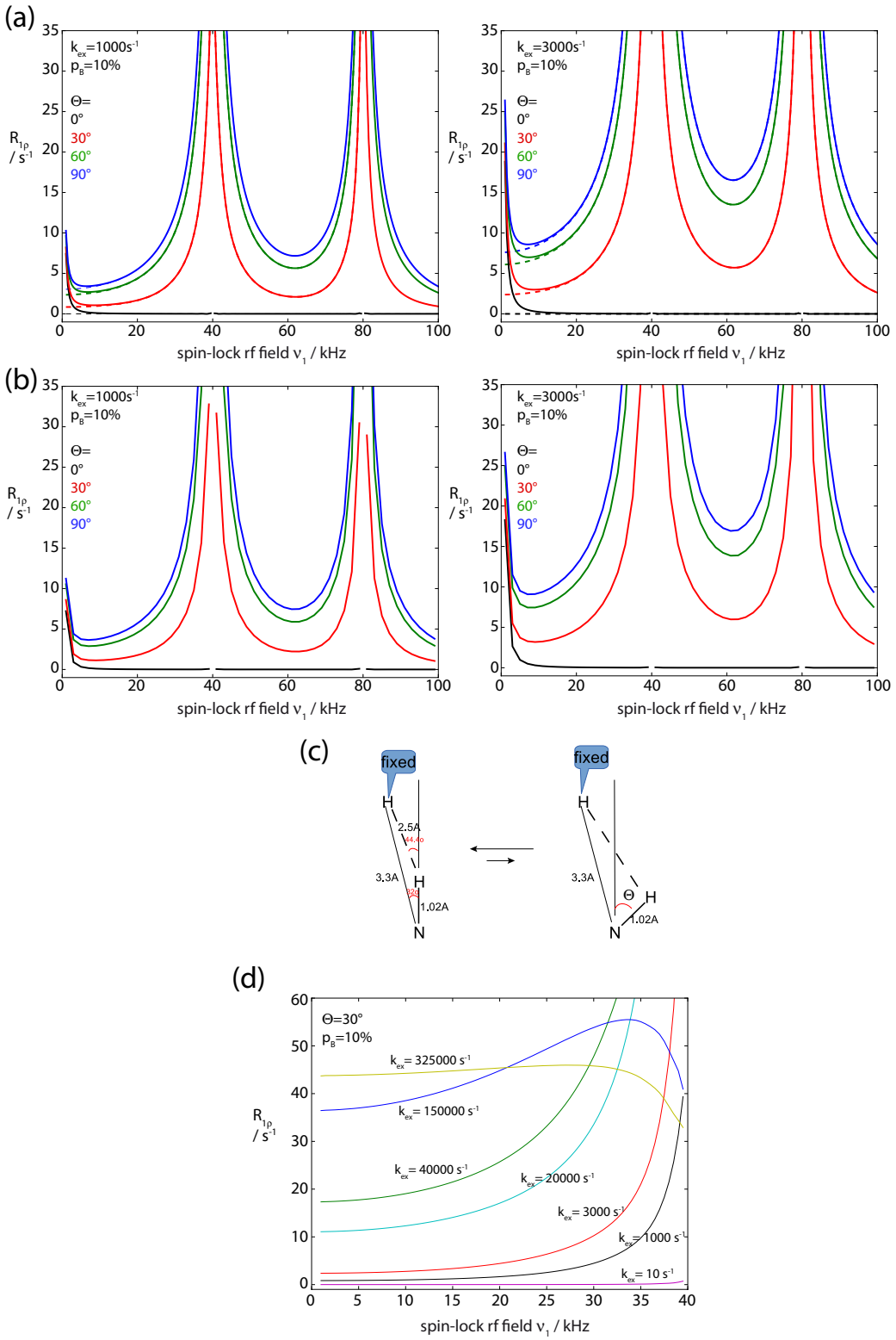

Figure S1. **Numerical simulations of $R_{1\rho}$ relaxation dispersion in a solid sample undergoing two-site conformational exchange and magic-angle spinning.** All simulations were performed as described above (page 4 of Supp. Info.). In panels (a) and (d), a two-spin system was assumed, as shown in Figure 1 of the main paper; for panel (b), a three-spin system was assumed, as drawn in panel (c), where one remote proton was assumed at a fixed position. Selected time-domain traces, which were used to obtain these fitted values, are shown in Figure S2.

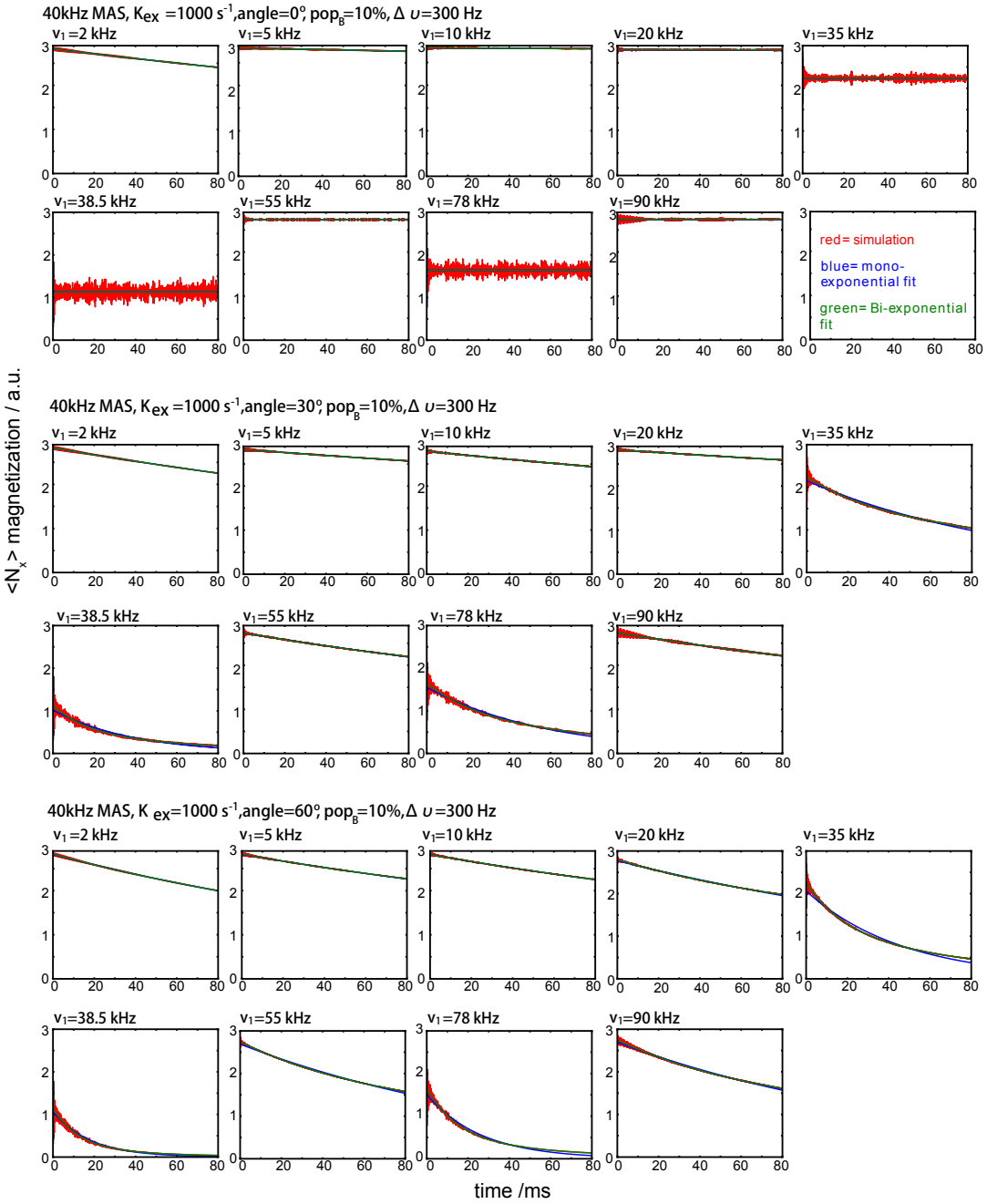

Figure S2, Part 1. Selected time-domain data of the numerical simulations. Shown are individual time traces from simulations of ^{15}N $R_{1\rho}$ decay from GAMMA, along with mono-exponential (blue) and bi-exponential (green) fit curves. Time scales of exchange, jump angles and rf field strengths are indicated. These data correspond to the data shown in Figure S1a.

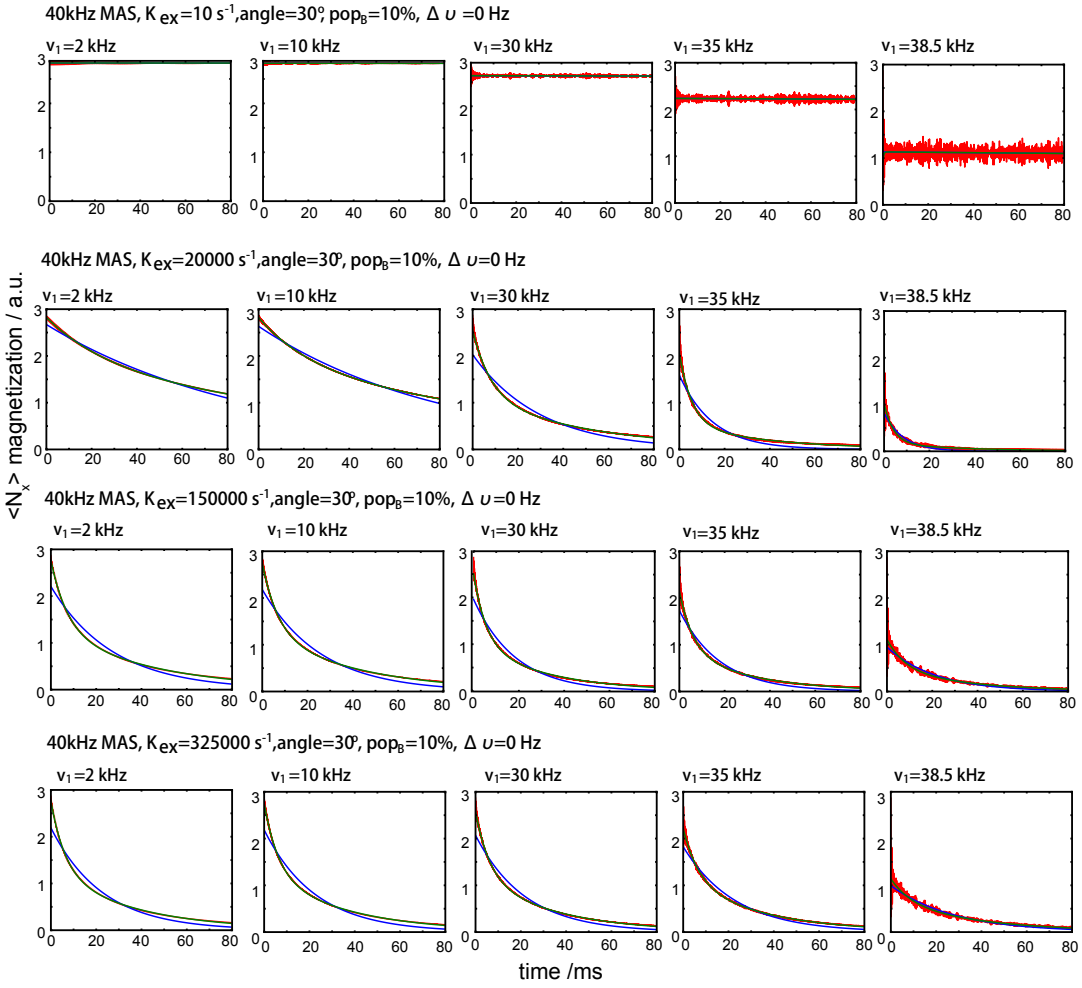

Figure S2, Part 2. Selected time-domain data of the numerical simulations. These data correspond to the simulations of different exchange rate constants, as shown in Figure S1d.

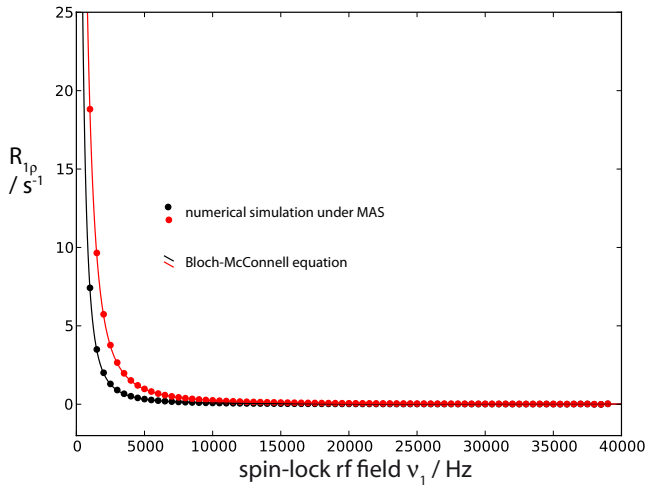

Figure S3. Comparison of Bloch-McConnell- and MAS-simulations.
Agreement of $R_{1\rho}$ RD profiles from explicit simulations under exchange and MAS (circles), and using the Bloch-McConnell formalism (solid lines), for the case that no angular fluctuations are involved. In all cases, a two-site exchange was assumed. The exchange parameters were: $\Delta\nu$=300 Hz. k_{ex}=1000 s^{-1} (black) and 3000 s^{-1} (red). The populations of the two exchanging states were assumed as 90%/10%. These data correspond to the values assumed in Figure 1.
In the GAMMA simulations, only isotropic chemical shift fluctuations were assumed, while the jump angle θ was set to zero. The agreement with the Bloch-McConnell treatment (which ignores the jump angle) is evident.

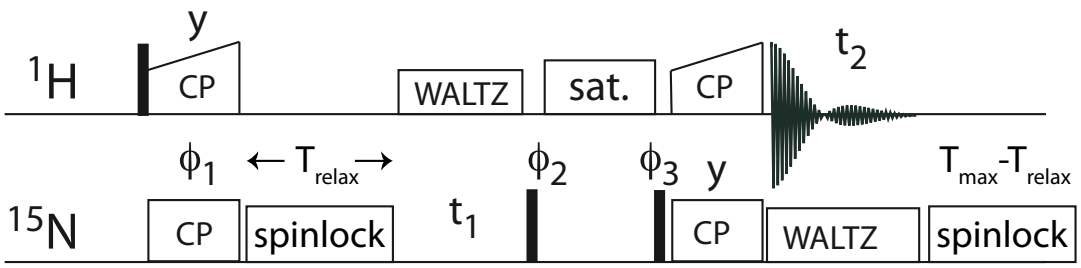

Figure S4. Pulse sequence used in this study.
CP: cross-polarization. sat.: water-saturation element, using a TPPM decoupling scheme to suppress solvent signal while the magnetization is stored on ^{15}N. The rf-induced temperature increase in the sample was kept constant for all relaxation delays by adding an additional spinlock of identical amplitude and a duration T_{max}-T_{relax}, where T_{max} is the maximum relaxation delay used.

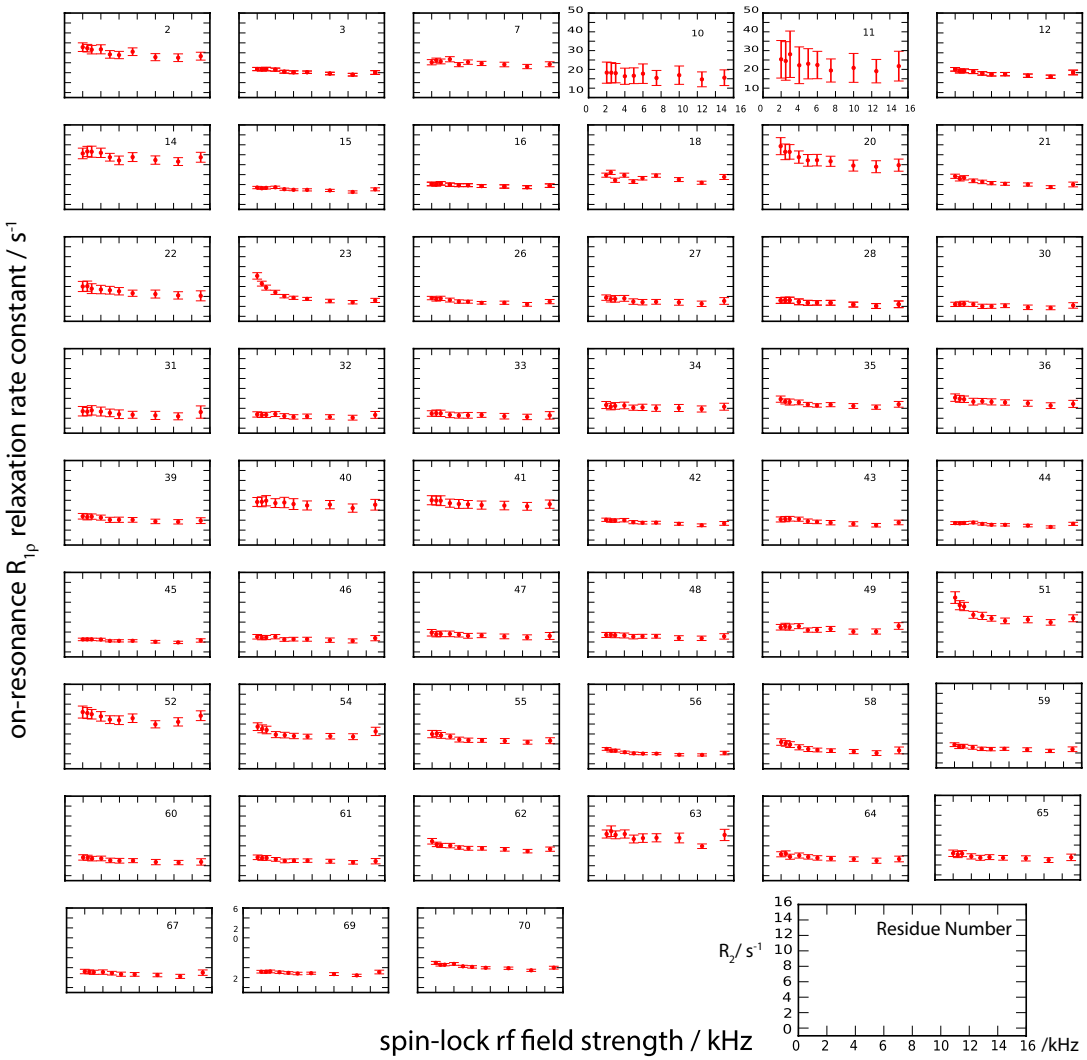

Figure S5. Experimental RD profiles for all observed resolved correlation peaks in ubiquitin, measured at 39.5 kHz MAS frequency. The axes labels are shown in the lower right panel only, except for residues 10 and 11, which have higher-than-average values of R1ρ because of extended nanosecond motion.[13]

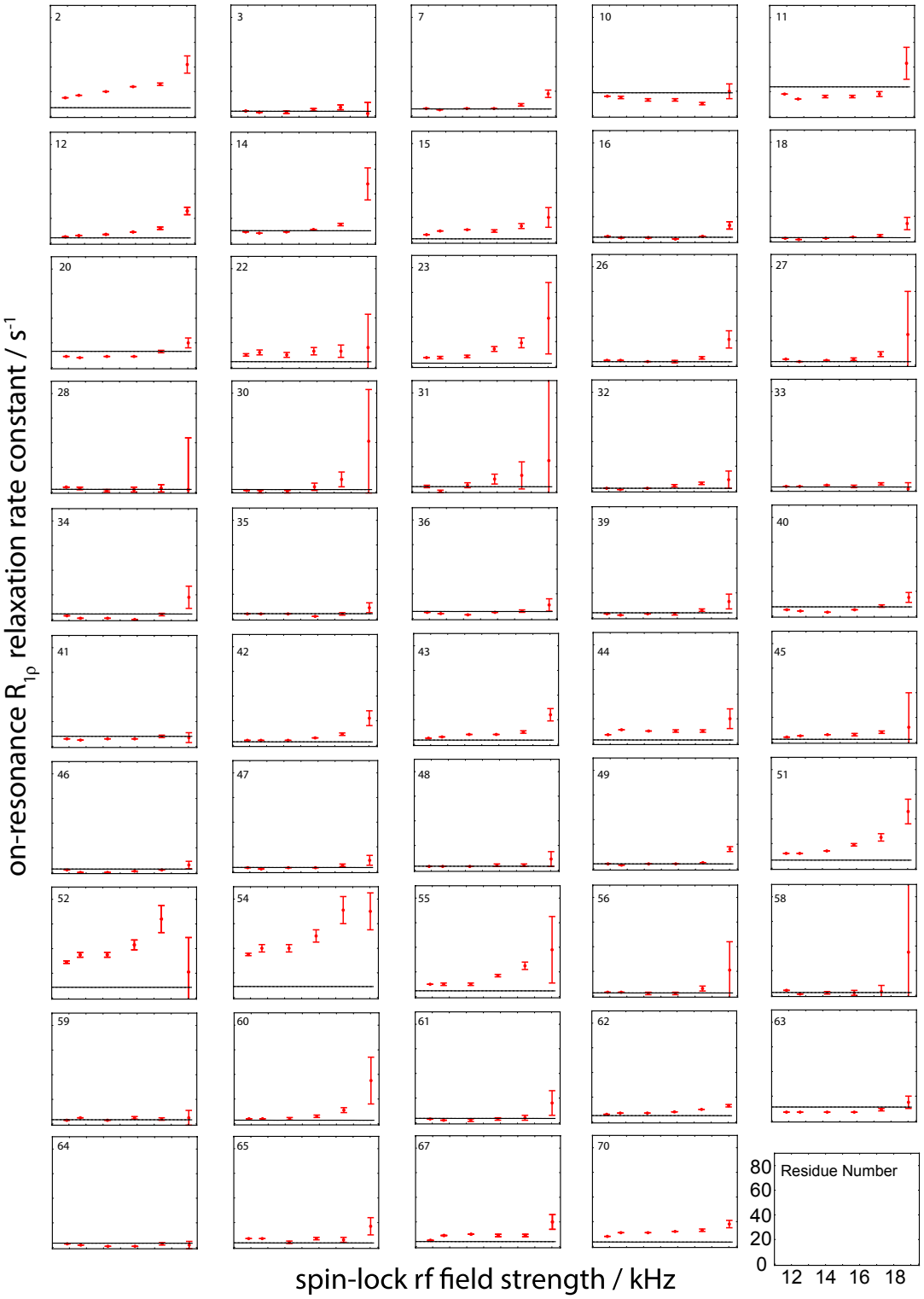

Figure S6. Experimental RD profiles for all observed resolved correlation peaks in ubiquitin, measured at 20 kHz MAS frequency.
Black lines indicate the value found at 39.5 kHz MAS and a spin-lock rf field strength of 15 kHz.

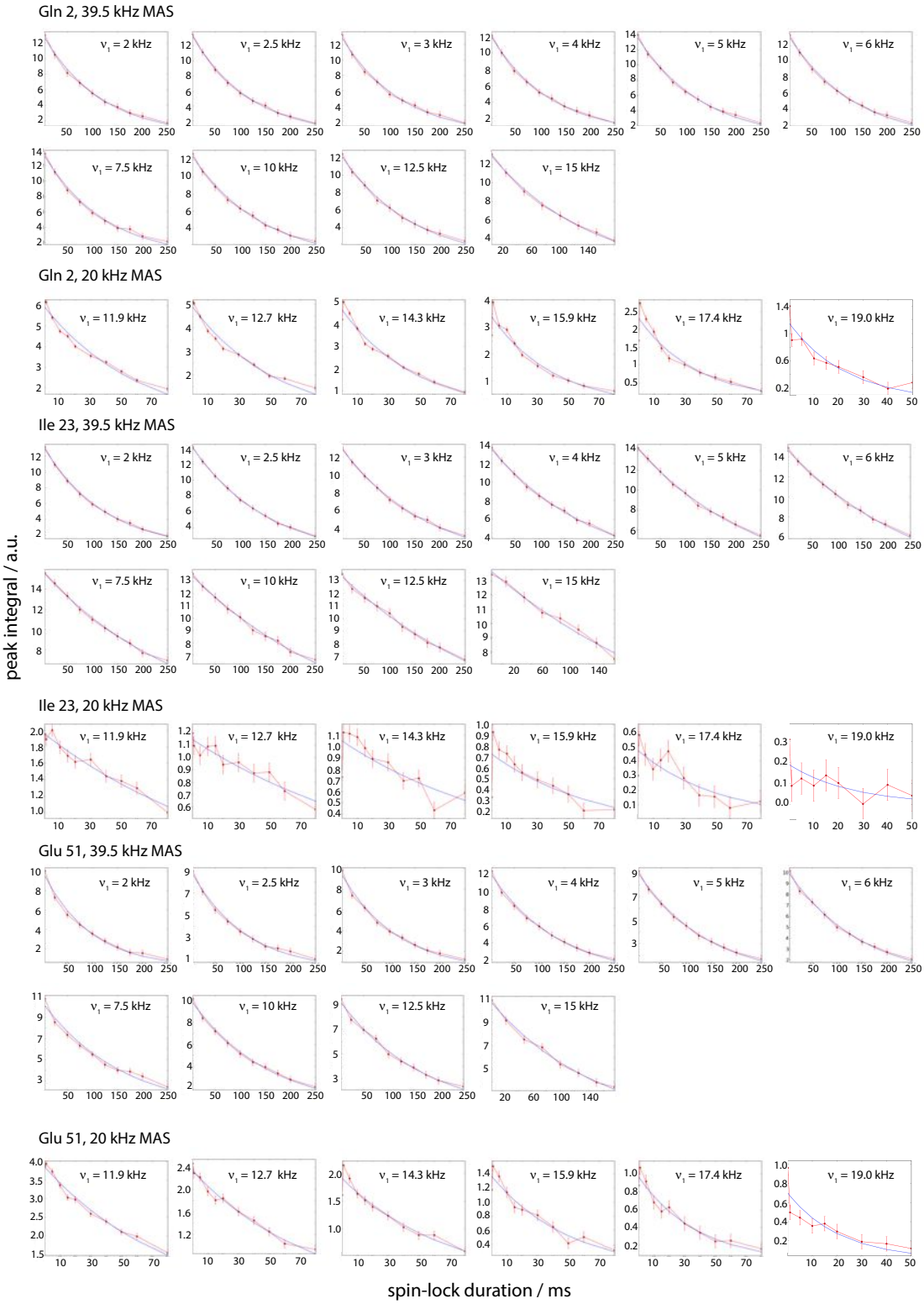

Figure S7. Examples of experimental ^{15}N $R_{1\rho}$ decay curves.

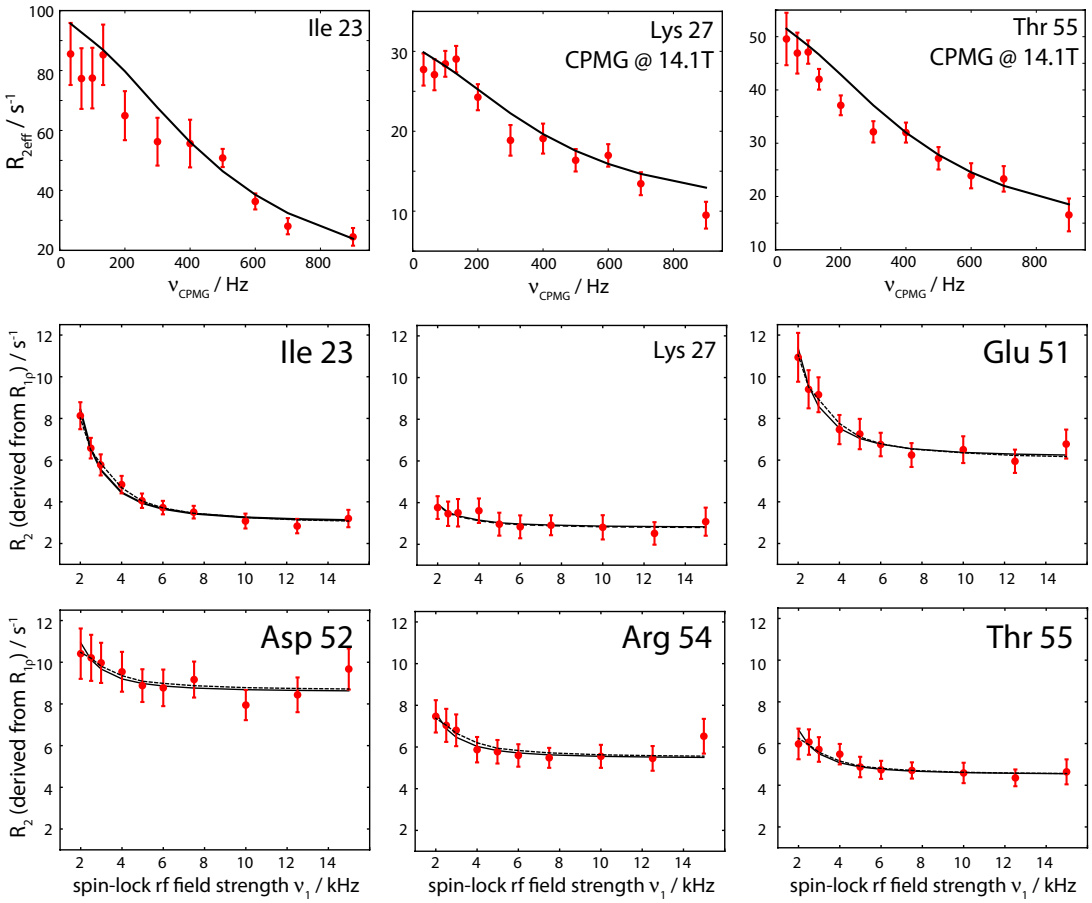

Figure S8. Bloch-McConnell fits of CPMG and $R_{1\rho}$-derived relaxation dispersion profiles.

Solid lines show the fit curves for a joint fit that includes all shown $R_{1\rho}$-derived RD curves and CPMG RD data for residues 23, 27, 55 (used in reference [8]) measured at 14.1 T. For comparison, dashed lines in the 6 lower panels show fits of $R_{1\rho}$-derived RD only, i.e. as shown in Figure 2a.

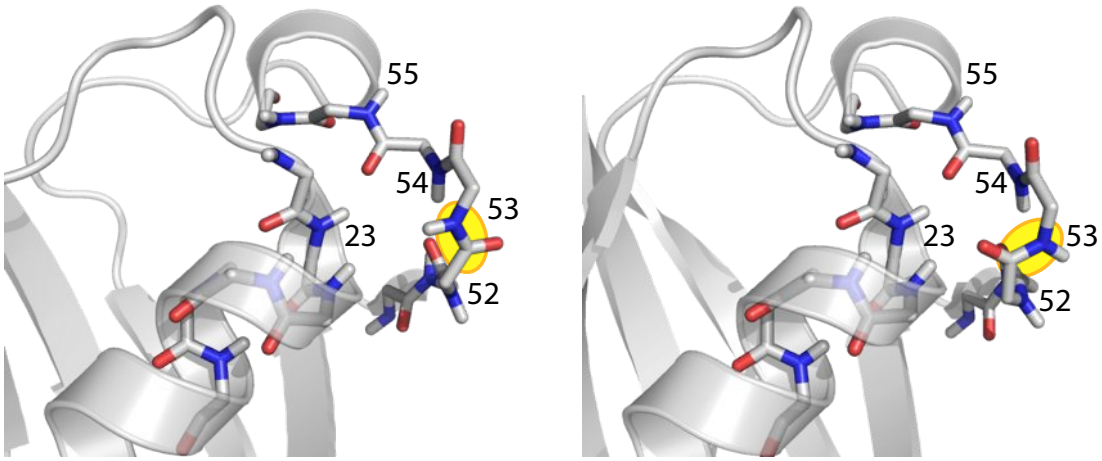

Figure S9. Comparison of crystal structures of ubiquitin.
Left: The structure of microcrystals obtained in methyl-pentane-diol, used in this study (pdb entry 3ONS). Right: Crystal structure reported in pdb entry 1UBI. Note the different orientation of peptide plane 52/53, highlighted in yellow. The two structures were aligned along all residues located in secondary structure elements (1-7, 13-17, 23-34, 42-45, 48-50, 57-59, 65-70).

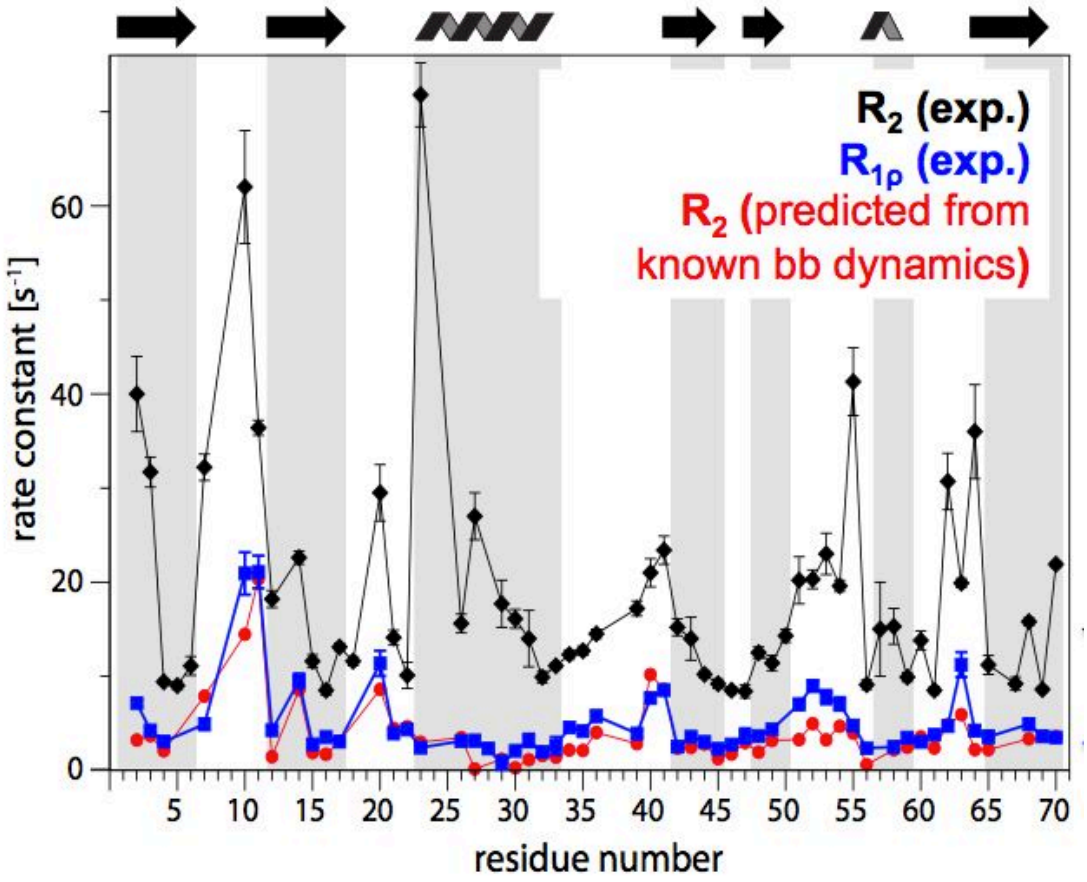

Figure S10. Comparison of ^{15}N R_2 and $R_{1\rho}$ rates in microcrystalline ubiquitin. Data points in red are back-calculated R_2 rate constants, based on the backbone dynamics that has been determined from a number of relaxation data and dipolar couplings[6]. Black data points show measured R_2 data from a simple spin-echo experiment measured at 57 kHz MAS frequency and 19.96 T static magnetic field strength on a sample that is fully deuterated, and where exchangeable hydrogen sites are back-protonated to 30 %.[14] The blue data set shows the (offset-corrected) $R_{1\rho}$ rate constants, obtained at a spin-lock field strength of 15 kHz.[13] This comparison shows clearly that the $R_{1\rho}$ rate constants are essentially only dependent on dynamics, while R_2 rate constants are systematically higher than predicted, showing that some dipolar dephasing contributes to these rates.[15]

Table S1. Fitted exchange parameters.

(a) Fit of $R_{1\rho}$ RD data only:

global kinetic parameters			
K_{eg}	8600±1700 s-1	Population	3.1±1.2%

Residue Specific parameters	
Residue	Δω (ppm)
23	5.63±0.6
27	2.55±0.7
51	5.63±0.6
52	3.54±1.4
54	3.55±1.0
55	3.43±0.9

(b) Fit of $R_{1\rho}$ RD and CPMG RD data (14.1 T):

global kinetic parameters			
k_{ex}	2900±140 s-1	Population	9.3±0.6%

Residue Specific parameters	
Residue	Δω (ppm)
23	5.12±0.2
27	2.23±0.2
51	5.04±0.8
52	3.36±0.7
54	3.23±0.8
55	3.21±0.2

References

(1) Igumenova, T.; McDermott, A.; Zilm, K.; Martin, R.; Paulson, E.; Wand, A. *J Am Chem Soc* **2004**, *126*, 6720.
(2) Thurber, K. R.; Tycko, R. *J Magn Reson* **2009**, *196*, 84.
(3) Delaglio, F.; Grzesiek, S.; Vuister, G.; Zhu, G.; Pfeifer, J.; Bax, A. *J Biomol NMR* **1995**, *6*, 277.
(4) Motulsky, H.; Christopoulos, A. **2003**, 1.
(5) Palmer, A. G.; Massi, F. *Chem Rev* **2006**, *106*, 1700.
(6) Schanda, P.; Meier, B. H.; Ernst, M. *J Am Chem Soc* **2010**, *132*, 15957.
(7) Baldwin, A. J.; Kay, L. E. *J Biomol NMR* **2013**.
(8) Tollinger, M.; Sivertsen, A. C.; Meier, B. H.; Ernst, M.; Schanda, P. *J Am Chem Soc* **2012**, *134*, 14800.
(9) Smith, S.; Levante, T.; Meier, B.; Ernst, R. *J Magn Reson* **1994**, *106*, 75.
(10) Edén, M. *Concepts in Magnetic Resonance Part A* **2003**, *17*, 117.
(11) Edén, M. *Concepts in Magnetic Resonance Part A* **2003**, *18*, 1.
(12) Cheng, V. B.; Suzukawa, H. H.; Wolfsberg, M. *J Chem Phys* **1973**, *59*, 3992.
(13) Haller, J. D.; Schanda, P. *J Biomol NMR* **2013**.
(14) Schanda, P.; Huber, M.; Verel, R.; Ernst, M.; Meier, B. H. *Angew Chem Int. Ed. Engl.* **2009**, *48*, 9322.
(15) Lewandowski, J. R.; Sass, H. J.; Grzesiek, S.; Blackledge, M.; Emsley, L. *J Am Chem Soc* **2011**, *133*, 16762.